Modeling and Optimizing Submerged Hollow Fiber Membrane Modules

S. Chang and A. G. Fane
UNESCO Center for Membrane Science and Technology, The University of New South Wales, Sydney 2052, Australia

S. Vigneswaran
Faculty of Engineering, University of Technology Sydney, Sydney 2007, Australia

The filtration behavior of submerged hollow fiber membranes with constant permeate flow operational mode was modeled on two different conditions: the maximum initial flux along the fiber is smaller than the critical flux ($J_{imax} < J_{cr}$); the maximum initial flux along the fiber is greater than the critical flux, but the averaged imposed flux is smaller than the critical flux ($J_{imax} > J_{cr}$ but $J_{mi} < J_{cr}$). When the maximum initial flux along the fiber is lower than the critical flux, no particle deposition occurs and the flux distribution can be characterized by a dimensionless parameter $\xi = 4LR_i^{-3/2}R_m^{-1/2}$. On the other hand, for $J_{mi} < J_{cr}$ and $J_{imax} > J_{cr}$, a steady state can be achieved after some initial deposition. The theoretical model shows that the filtration resistance caused by the initial deposition can be affected by J_{mi}/J_{cr} and fiber characteristics (L, R_i and R_m) and becomes significant for narrow and long fibers with a high J_{mi}/J_{cr}. The models were also used to determine the optimal fiber length and radius for the submerged hollow fiber module. The simulation suggests that the optimal fiber lumen radius for fiber lengths of 0.5−3 m is 0.2−0.35 mm. These results should be relevant to the design of submerged hollow fiber modules.

Introduction

Hollow fiber membranes have been employed for a variety of separations (for example, reverse osmosis, ultrafiltration, and microfiltration) and as bioreactors (with immobilized enzymes for mammalian cell culture). The hollow fiber module could be a hollow fiber cartridge that consists of fibers sealed into a cylindrical casing, forming a shell-and-tube configuration or a bundle of fibers in a tank as in the submerged system used for membrane bioreactors (MBRs). Most hollow fiber cartridges are operated in constant pressure mode where constant shell or tube side pressure is applied as the process driving force, while for the submerged system the permeate is usually pumped out of the fiber lumen at a constant flow rate (Figure 1).

Modeling filtration behavior of hollow fibers is important for improving operation and design of the hollow fiber system. The hydrodynamic environment in the hollow fiber module depends on the flows in three regions: flow in the

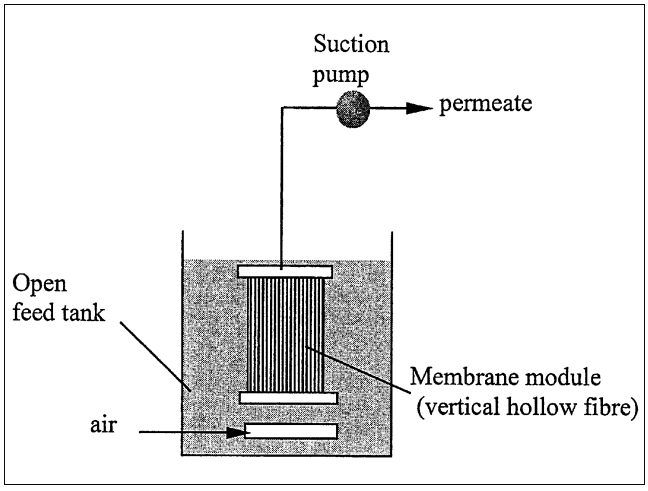

Figure 1. Submerged hollow fiber module (coordinate system shown in Figure 3).

Correspondence concerning this article should be addressed to A. G. Fane.

fiber lumen, inside the membrane and outside the membrane. Apelblat et al. (1974) provided a fundamental mathematical analysis for fluid exchange in capillary-tissue systems for a low viscosity fluid. They modeled the capillary wall as a thin membrane and the surrounding tissue as a porous bed. Simplified Navier-Stokes equations and Darcy's law were applied to describe flow in the fiber lumen and in the tissue region, respectively. Based on the basic method provided by Apelblat et al. (1974), Kelsey et al. (1990) developed analytical expressions for the radial and axial velocities and pressure profiles in a hollow-fiber bioreactor with immobilized enzymes or cells by solving the coupled momentum and continuity equations in the fiber lumen, matrix, and surrounding shell. Bruining (1989) developed a general model to predict the pressure drop and the magnitude and direction of flows in a hollow fiber cartridge for different operational modes by treating the flow in the fiber lumen as a Poiseuille flow. Doshi et al. (1977) modeled the flow in a hollow fiber RO cartridge and optimized the fiber length and radius through maximizing the permeate flow rate per unit shell volume. Their results showed that the performance of the hollow fiber cartridge can be significantly improved by optimizing fiber length and radius. Recently, Serra et al. (1998) simulated dead-end ultrafiltration (no back-transport) in a hollow fiber cartridge using a semi-analytical model and Hagen-Poiseuille law to describe the pressure drop outside and inside the hollow fibers, respectively. The model considered filtration with and without fouling and was used to optimize the design parameters of the module and predict the net rate of production of the module during an operating cycle.

Although the previous work provides a good base for modeling flow in a hollow fiber, the models developed are not applicable to the submerged system due to different boundary conditions which depend on operation mode, flow arrangement, and module configuration. A model for submerged hollow fiber membranes was developed in our previous article, but it is only applicable to filtration without deposition (Chang and Fane, 2001). In the present work, we analyze the fouling behavior of submerged hollow fibers with different imposed fluxes. The basic conditions under which a steady operation can be achieved are identified according to the concept of the critical flux and the initial distribution of the flux along the fiber. Theoretical models are developed to simulate filtration resistance and axial pressure drop along the fiber at steady state. These models can be used to analyze the effect of the fiber radius and length on filtration behavior of the hollow fiber. The optimal hollow fiber length and radius for the submerged module are determined through maximizing the permeate flow rate per unit cross section area and per unit axial pressure drop along the fiber.

Background and Basic Assumptions

Concept of critical flux

The critical flux for cross flow filtration can be regarded as the flux at which the convection of particles to the membrane surface caused by the permeate flow is balanced by the back transport of particles from the membrane induced by the shear flow. This concept implies that particle deposition can be avoided by controlling the flux below a critical value (Field et al., 1995; Li et al., 1998). For filtration with crossflow, particle back transport may be attributed to the mechanisms of shear induced diffusion and inertial lift (Belfort et al., 1994). For the submerged hollow fiber module, the main hydrodynamic technique used to control particle deposition is bubbling outside the fibers. Although it is difficult to mathematically describe the relationship between bubbling and particle back-transport, the fact that submerged systems can be operated with a stable flux of 10–20 L/m^2 h for a long time without frequently cleaning shows that bubbling is effective in controlling particle deposition on hollow fibers (Ohmori et al., 1999; Günder and Krauth, 1998; Ueda and Hata, 1999). The back transport of particles for the submerged system may be caused by turbulent wakes, fiber shaking, and the recirculation of the bioreactor liquid caused by bubbling. The critical flux along the fiber depends on the local hydrodynamic environment. We assume the local critical flux caused by bubbling is constant along the fiber (this is a necessary simplification until more information is available on axial variations in bubble properties and fiber movement). Thus, the fouling behavior mainly depends on the flux distribution along the fiber, which itself depends on the distribution of suction pressure driving force. Modeling of this distribution is considered in the section titled "Model Development."

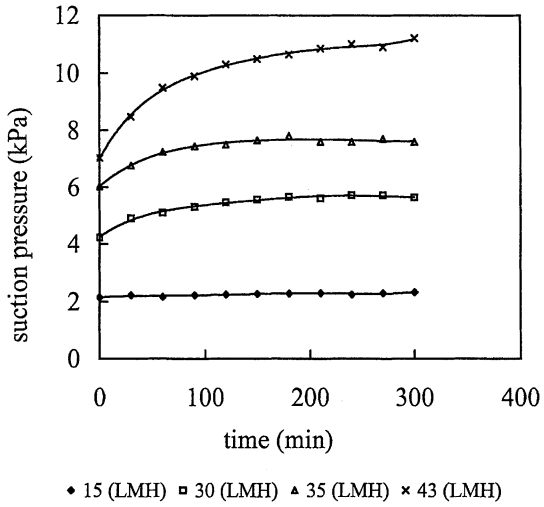

Figure 2. Filtration behavior of submerged hollow fiber module with different imposed fluxes (V_g = 1.8 L/min).

Fouling behavior of hollow fibers

Figure 2 shows the filtration curves for filtration with a lab-scale submerged module with different imposed fluxes. The module consisted of 0.2 μm hollow fibers with an inner radius of 0.39 mm and a length of 0.51 m. The feed was 5 g/L yeast suspension. In the experiments, the flux was set at a constant value by the permeate pump and the performance was assessed by measuring the suction pressure. From the figure, it can be seen that when the flux was set at 15 L/m^2 h, no suction pressure increase was observed over a filtration time of 5 h. For 30 and 35 L/m^2 h, there was an initial increase in suction pressure, but a steady state was established after about 100 min. When the imposed flux was set at 43

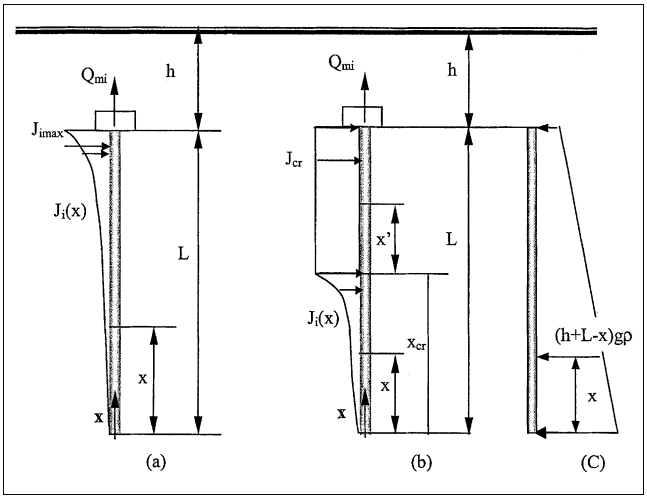

Figure 3. Flux distribution at steady state for different imposed flux conditions.

(a) $J_{i\max} < J_{cr}$; (b) $J_{mi} < J_{cr}$ and $J_{i\max} > J_{cr}$; (c) exterior pressure distribution.

L/m^2 h, no steady state was observed even after 5 h filtration. Combining these experimental phenomena with the concept of the critical flux and the initial distribution of flux along the fiber, we suggest the following scenarios for filtration with the submerged hollow fiber (for convenience, all flux is based on the inner area of the hollow fiber which maintains constant in filtration):

The maximum initial flux is smaller than the critical flux ($J_{i\max} < J_{cr}$). No initial suction pressure rise occurs and the performance maintains stable from the beginning of filtration, as with 15 L/m^2 h in Figure 2. For this situation, the flux distribution is inhomogeneous along the fiber as shown in Figure 3a.

The maximum initial flux is greater than the critical flux but the average imposed flux is smaller than the critical flux. ($J_{i\max} > J_{cr}$ & $J_{mi} < J_{cr}$). A steady state can be achieved after an initial increase in suction pressure as with the 30 and 35 L/m^2 h data in Figure 2. The initial deposition will occur on the local area where the initial flux is higher than the critical flux, that is, near the lumen outlet where the driving force is maximum. This results in an increased filtration resistance in this area, which, in turn, decreases the local flux. For constant flux operation mode, the deposition will lead to an increase in suction pressure which tends to adjust the flux distribution to compensate for the loss of the permeate flow caused by local flux decline. Although it is difficult to describe the progress of adjustment, the fact that a steady state can be built up after some initial increase in suction pressure which indicates that the adjustment will finally reduce the local flux from above the critical flux to the critical flux. Assuming the adjustment of flux distribution caused by the initial deposition is continuous along the fiber with time, the flux distribution at the steady state should be of the pattern shown in Figure 3b. In this case the flux is uniform and equal to the critical flux in a region from the outlet of the fiber to some point, while, beyond this region, the flux is lower than the critical flux. This means that the initial deposition only occurs on some portion of the fiber close to the outlet.

The averaged imposed initial flux is greater than the critical flux ($J_{mi} > J_{cr}$). Suction pressure increases with time as with the case of 43 L/m^2 h in Figure 2. A steady state would not be reached until the growing cake thickness drops the local external surface-based flux to the critical flux, or before that the high filtration resistance stops the filtration.

For a practical submerged hollow fiber system, it is necessary to control the average flux below the critical flux in order to obtain a stable performance. Our modeling will focus on this situation.

Model Development

Basic equations

For flow in a hollow fiber, the Navier-Stokes equations can be simplified by neglecting the inertial forces caused by acceleration due to the very low ratio of the radial velocity to axial velocity. Thus, for the model fibers which have a closed bottom and an open top, and the permeate flow from outside to inside as shown in Figure 3, the axial and radial velocities in the hollow fiber can be expressed as (Apelblat, 1974)

$$u(x,r) = -\frac{1}{4\mu}\left(\frac{dp}{dx} + g\rho\right)\left(R_i^2 - r^2\right) \tag{1}$$

$$v(x,r) = \frac{1}{16\mu}\frac{d^2p}{dx^2}\left(2R_i^2 r - r^3\right) \tag{2}$$

Since we have two expressions with 3 unknowns, constitutive relationships and boundary conditions are needed to rigorously solve Eqs. 1 and 2.

Filtration with $J_{imax} < J_{cr}$

When $J_{i\max}$ is lower than the critical flux, no deposition occurs and the filtration resistance stays constant throughout the filtration. The filtration resistance can be regarded equal to the membrane resistance which can be determined through the filtration of pure water. The models of pressure and flux distribution for this situation have been developed in our previous article where the boundaries were determined according to interface continuity, one-end closed situation ($u(0,r) = 0$), and mass balance (Chang and Fane, 2001) so that

$$p(x) = (h + L - x)g\rho - \frac{\mu\lambda R_m J_{mi} L}{e^{\lambda L} - e^{-\lambda L}}\left(e^{\lambda x} + e^{-\lambda x}\right) \tag{3}$$

where the first term on the righthand side of Eq. 3 is the local hydrostatic pressure and the second term is the lumen pressure drop due to flow

$$J_i(x) = \frac{\lambda L J_{mi}}{e^{\lambda L} - e^{-\lambda L}}\left(e^{\lambda x} + e^{-\lambda x}\right) \tag{4}$$

where

$$\lambda = 4R_i^{-3/2}R_m^{-1/2}$$

Filtration with $J_{mi} < J_{cr}$ and $J_{imax} > J_{cr}$

Under the conditions of $J_{mi} < J_{cr}$ and $J_{i\max} > J_{cr}$, a steady state can be achieved after an initial deposition. Figure 3b shows the characteristics of flux distribution at the steady state. Models can be developed for describing flux or pressure distribution in different regions: $0 \le x \le x_{cr}$, and $x_{cr} \le x \le L$, where x_{cr} represents the fiber length over which the flux is lower than the critical flux.

Flux and Pressure Distribution in the Range of $0 \le x \le x_{cr}$. Since the local flux in the range of $0 \le x \le x_{cr}$ is lower than the critical flux, no deposition takes place in this range. The pressure and flux distribution can be described by Eqs. 3 and 4 or

$$p(x) = (h + L - x)g\rho - \frac{\mu\lambda R_m J'_{mi} x_{cr}}{e^{\lambda x_{cr}} - e^{-\lambda x_{cr}}}(e^{\lambda x} + e^{-\lambda x}) \quad (5)$$

$$J(x) = \frac{\lambda J'_{mi} x_{cr}}{e^{\lambda x_{cr}} - e^{-\lambda x_{cr}}}(e^{\lambda x} + e^{-\lambda x}) \quad (6)$$

where J'_{mi} is the average flux over the length x_{cr}.

According to the mass balance, the total permeate flow rate from the fiber lumen equals the sum of the permeate flow from both regions of $0 \le x \le x_{cr}$, and $x_{cr} \le x \le L$ and J'_{mi} can be calculated from

$$J'_{mi} = \frac{J_{mi}L - J_{cr}(L - x_{cr})}{x_{cr}} \quad (7)$$

Assuming interface continuity, we can set $J(x_{cr}) = J_{cr}$ or from Eq. 6

$$\lambda x_{cr} J'_{mi} \coth(\lambda x_{cr}) = J_{cr} \quad (8)$$

Then, using Eq. 7 to replace J'_{mi}, Eqs. 8, 5 and 6 can be rewritten as

$$\lambda[FL - (L - x_{cr})]\coth(\lambda x_{cr}) = 1 \quad (9)$$

$$p(x) = (h + L - x)g\rho - \frac{\mu\lambda R_m[J_{mi}L - J_{cr}(L - x_{cr})]}{e^{\lambda x_{cr}} - e^{-\lambda x_{cr}}}(x^{\lambda x} + e^{-\lambda x}) \quad (10)$$

$$J(x) = \frac{\lambda[J_{mi}L - J_{cr}(L - x_{cr})]}{e^{\lambda x_{cr}} + e^{-\lambda x_{cr}}}(e^{\lambda x} - e^{-\lambda x}) \quad (11)$$

where

$$F = J_{mi}/J_{cr}$$

For a given hollow fiber and average imposed flux and critical flux, x_{cr} can be determined by Eq. 9. Then, Eqs. 10 and 11 can be used to calculate pressure and flux distribution in the region of $0 \le x \le x_{cr}$ at the steady state for a given fiber, imposed permeate flow rate, and critical flux.

Pressure Distribution in the Range of $x_{cr} \le x \le L$ $(0 < x' \le L - x_{cr})$. At the steady state, the flux distribution in the range of $x_{cr} \le x \le L$ $(0 < x' \le L - x_{cr})$ is uniform and equals J_{cr} (Figure 3b). Assuming that the radial component of velocity is continuous across the interface between the membrane and the porous medium, we have $v(x', R_i) = -J_{cr}$ $(0 < x' \le L - x_{cr})$. Combining such boundary conditions with Eq. 2

$$\frac{d^2p}{dx'^2} = -\frac{16\mu J_{cr}}{R_i^3} \quad (12)$$

then

$$\frac{dp}{dx'} = -\frac{16\mu J_{cr}}{R_i^3}x' + c_1 \quad (13)$$

$$p(x') = -\frac{8\mu J_{cr}}{R_i^3}x'^2 + c_1 x' + c_2 \quad (14)$$

For Eq. 14, the boundary conditions can be determined as

$$p(x_{cr}^-) = p(x_{cr}^+) \quad (15)$$

$$\left.\frac{dp}{dx}\right|_{x = x_{cr}^-} = \left.\frac{dp}{dx}\right|_{x = x_{cr}^+} \quad (16)$$

Then the constant C_1 and C_2 in Eq. 14 can be determined as

$$c_1 = -g\rho - \mu\lambda^2 R_m[J_{mi}L - J_{cr}(L - x_{cr})] \quad (17)$$

$$c_2 = (h + L - x_{cr})g\rho - \mu\lambda R_m[J_{mi}L - J_{cr}(L - x_{cr})]\coth(\lambda x_{cr}) \quad (18)$$

$p(x')$ can be determined by combining Eqs. 14, 17, and 18.

The distribution of filtration resistance in this region can be determined by the filtration equation

$$R_t(x') = R_m + R_c = \frac{(h + L - x_{cr} - x')g\rho - p(x')}{\mu J_{cr}} \quad (19)$$

Discussion

Models for filtration without deposition

Equations 3 and 4 describe the flux distribution along the fiber without deposition. These models are applicable to the prediction of the initial flux distribution along the fiber for a given averaged imposed flux and fiber. Figure 4 shows the simulated flux distribution for filtration with different imposed fluxes using these models. The calculation shows that the flux increases with x and reaches its maximum at the outlet of the fiber. From the figure, it can be seen that, although the maximum flux increases with the increase in the average imposed flux, the $J(x)/J_{mi}$ is independent of the value of J_{mi} and is specified for a given fiber diameter, length, and resistance.

The inhomogeneity of the initial flux distribution along the fiber can be characterized by $J_{i\max}/J_{mi}$ as well as L_h/L, where L_h is the length of the fiber over which the initial local flux is higher than the average flux. Our previous modeling has indicated that $J_{i\max}/J_{mi}$, and L_h/L are functions of a dimensionless coefficient $\lambda L = \xi = 4LR_i^{-3/2}R_m^{-1/2}$ (Chang and Fane, 2001). Figure 5 shows the simulated effect of the dimension-

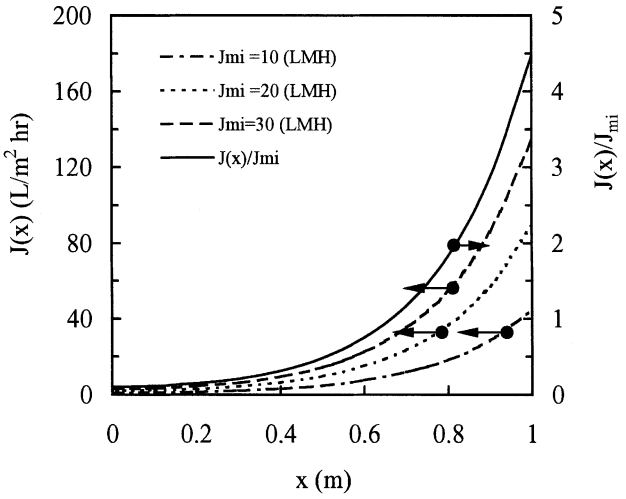

Figure 4. Simulated flux distribution along a fiber.

Simulation conditions: $R_i = 0.2$ mm, $R_m = 10^{11}$ L/m, $L = 1$ m.

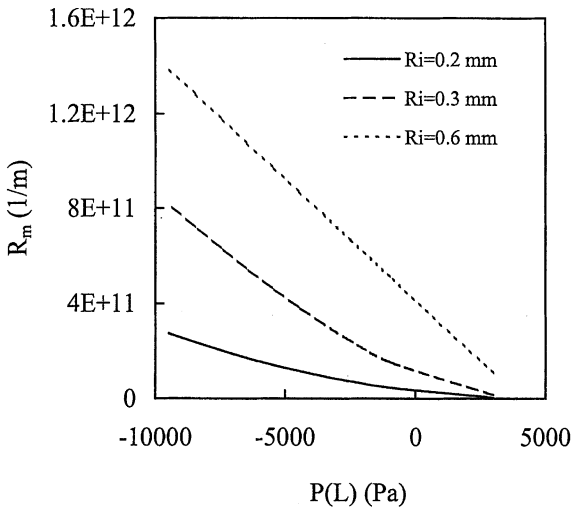

Figure 6. Simulated relationship between membrane resistance and pressure at the outlet of the fiber.

Simulation conditions: $L = 2$ m, $J_{mi} = 9.7 \times 10^{-6}$ m/s, $h = 0.5$ m, $g = 9.8$ m/s^2, $\rho = 1{,}000$ kg/m^3, $\mu = 0.001$ Ns/m^2.

less parameter (ξ) on $J_{i\max}/J_{mi}$ and L_h/L. According to the simulated results, we can see that when $\xi > 2$, the relationship between ξ and $J_{i\max}/J_{mi}$ becomes almost linear and $J_{i\max}$ can be estimated by the approximate function $J_{i\max} = \xi J_{mi}$. Figure 5 also indicates that L_h/L decreases with the increase in the value of ξ. Thus, as the fiber radius is reduced and the fiber length is increased, the initial flux distribution becomes more inhomogeneous.

Another important application of the models for no cake filtration is to estimate the membrane resistance of the hollow fiber. For hollow fiber membranes, the TMP changes along the fiber, and the direct measurement can only determine the pressure at the outlet of the fiber rather than the TMP. Equation 3 can be used to relate the pressure at the fiber end to the membrane resistance by setting $x = L$

$$p(L) = hg\rho - \mu\lambda R_m J_{mi} L \coth(\lambda L) \qquad (20)$$

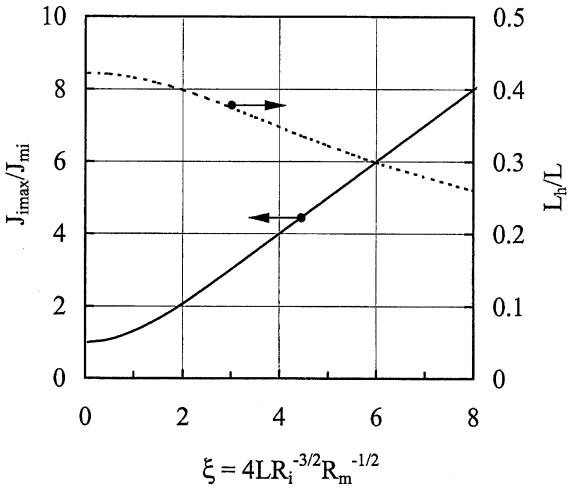

Figure 5. Simulated ξ-J_{imax}/J_{mi} and ξ-L_h/L relationship.

For a given fiber, average imposed flux, and the corresponding measured outlet pressure, the membrane resistance can be calculated from Eq. 20. Figures 6 and 7 show the simulated relationship between membrane resistance and the end-pressure with fibers of a different radius and length, respectively. From these figures, we can see that the relationship between the end pressure and membrane resistance is not linear for small and long fibers. However, the relationship between end pressure and membrane resistance tends to be linear for long fibers with a large radius (for example, $R_i = 0.6$ mm, $L = 2$ m), or for narrow fibers with a short length ($R_i = 0.3$ mm, $L = 0.5$ m) due to the decreased effect of inhomogeneity of the flux distribution under these conditions.

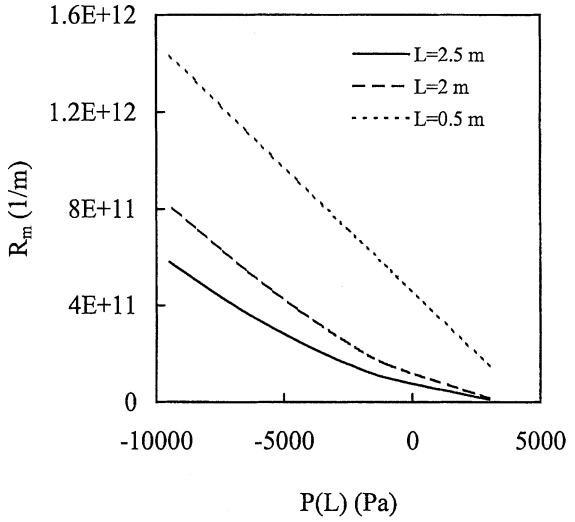

Figure 7. Simulated relationship between membrane resistance and pressure at the outlet of the fiber.

Simulation conditions: $R_i = 0.0003$ mm, $J_{mi} = 9.7 \times 10^{-6}$ m/s, $h = 0.5$ m, $g = 9.8$ m/s^2, $\rho = 1{,}000$ kg/m^3, $\mu = 0.001$ Ns/m^2.

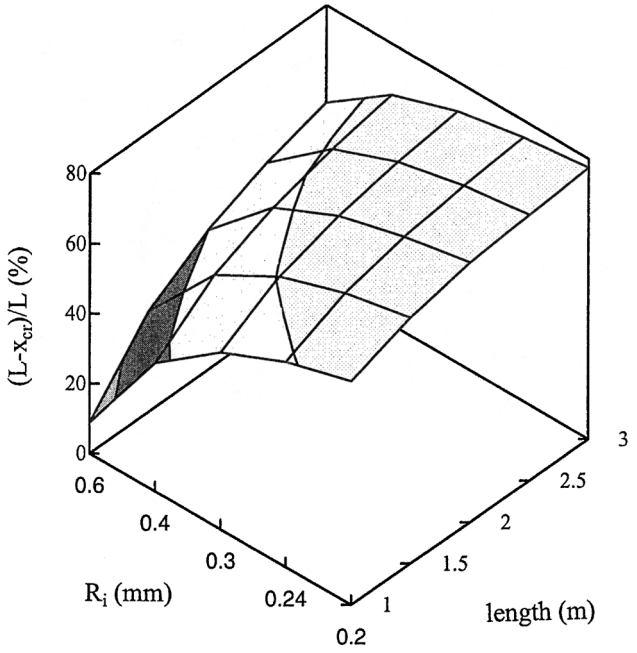

Figure 8. Simulated effect of fiber radius and length on $(L-x_{cr})/L$.

Simulation conditions: $J_{mi}/J_{cr} = 0.85$, $R_m = 10^{11}$ L/m.

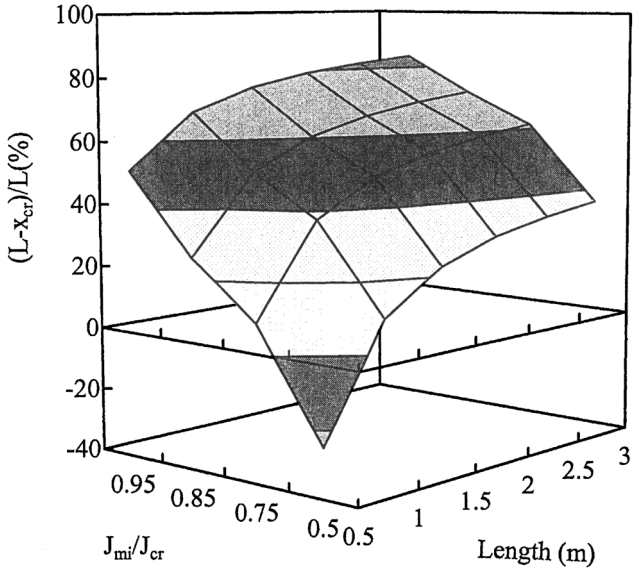

Figure 10. Simulated effect of fiber length and J_{mi}/J_{cr} on $(L-x_{cr})/L$.

Simulation conditions: $R_i = 0.0003$ m, $R_m = 10^{11}$ l/m.

Filtration with $J_{mi} < J_{cr}$ & $J_{imax} > J_{cr}$

When the maximum flux is higher than the J_{cr}, initial deposition occurs on some local membrane surface. At the steady state, the portion of fiber with deposition or $(L - x_{cr})$ depends on J_{mi}/J_{cr}, fiber length, radius, and membrane permeability (Eq. 9). Figures 8–10 show the effect of fiber radius, length, and J_{mi}/J_{cr} on $(L - x_{cr})/L$ (the proportion of fiber length with deposition). The simulation shows that the value of $(L - x_{cr})/L$ increases with a decrease in fiber diameter and an increase in fiber length and J_{mi}/J_{cr}. Comparing the effect of the fiber radius for short and long fibers on $(L - x_{cr})/L$ (Figure 8), or high and low J_{mi}/J_{cr} (Figure 9), it can be noted that the effect of radius decreases for long fibers or high J_{mi}/J_{cr}, respectively. Similar tendencies can also be observed with the effect of fiber length and J_{mi}/J_{cr} (Figure 10). These results imply that the portion of fiber with deposition at the steady state tends to be dominated by a small radius, or large length, or high J_{mi}/J_{cr}. The negative values of $(L - x_{cr})/L$ in Figures 9 and 10 imply that the maximum initial flux at the fiber end is lower than the critical flux under the related conditions (low J_{mi}/J_{cr} and short length). Obviously, the minimum value of $(L - x_{cr})/L$ must be zero.

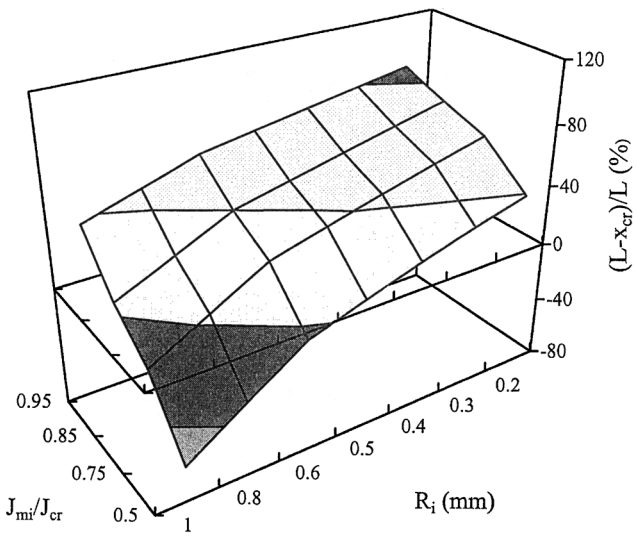

Figure 9. Simulated effect of fiber radius and J_{mi}/J_{cr} on $(L-x_{cr})/L$.

Simulation conditions: $L = 2$ m, $R_m = 10^{11}$ l/m.

Figure 11 shows the resistance distribution along the fiber at the steady state. There is no deposition in the region of $x < x_{cr}$, so the filtration resistance equals the membrane resistance ($R_m = 10^{11}$ m^{-1}). For $x > x_{cr}$, the resistance increases with x due to the increasing initial flux in this direction and reaches the maximum at the outlet of the fiber. Comparing the filtration resistance with fibers of a different radius, it can be seen that the filtration resistance increases with a decrease in fiber diameter. A practical implication of the axial distribution of cake resistance is that when back flushing is used to affect membrane cleaning, the backflow will take the path of least resistance with preference for the cake-free region. Up to 5 to 10 times more back flow could initially pass through these regions than through the most caked regions. This may explain our recent experimental observations on the effect of imposed flux on the effectiveness of back flushing, and the buildup of membrane resistance (Parameshwaran et al., 2001).

The energy required for removing the permeate flow out of the lumen can be assessed through the pressure drop along the fiber. Figure 12 shows the effect of fiber inner radius and fiber length on the pressure drop per unit length or $[P(I) - P(L)]/L$. The simulation indicates that small and long fibers

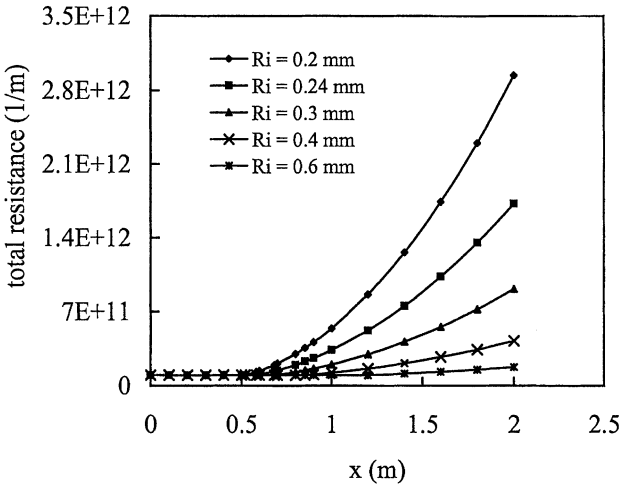

Figure 11. Simulated resistance distribution along fibers at steady state for filtration with $J_{mi} < J_{cr}$ and $J_{imax} > J_{cr}$.

Simulation conditions: $J_{mi}/J_{cr} = 0.85$, $J_{cr} = 5.56 \times 10^{-6}$ m/s, $L = 2$ m, $R_m = 10^{11}$ (l/m), $h = 0.5$ m, $g = 9.8$ m/s^2, $\rho = 1{,}000$ kg/m^3, $\mu = 0.001$ Ns/m^2.

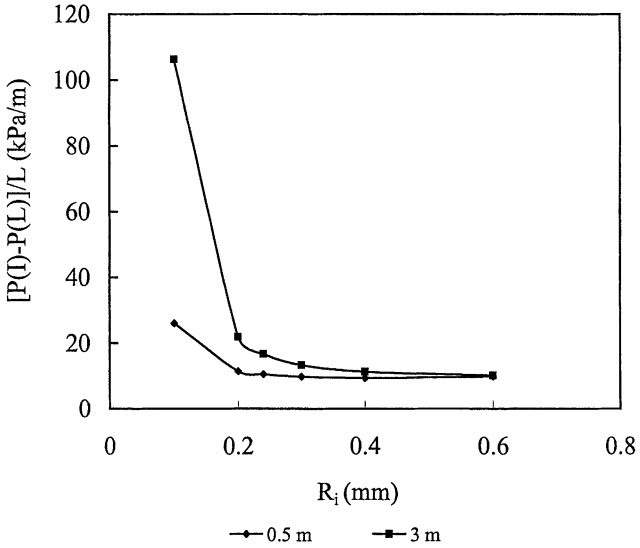

Figure 13. Simulated effect of fiber radius and length on $[P(I)-P(L)]/L$ for 0.5 m and 3 m long fibers.

Simulation conditions: $J_{mi}/J_{cr} = 0.85$, $J_{cr} = 5.56 \times 10^{-6}$ m/s, $R_m = 10^{11}$ (l/m), $h = 0.5$ m, $g = 9.8$ m/s^2, $\rho = 1{,}000$ kg/m^3, $\mu = 0.001$ Ns/m^2.

lead to higher axial pressure drop. A sharp increase in pressure drop is observed for fibers with $R_i < 0.2$ mm. Figure 13 shows the difference in pressure drop per unit length between 0.5 and 3 m long fibers for a different inner radius. It shows that the effect of fiber length increases with a decrease in fiber radius and sharply increases in the range of $R_i < 0.2$ mm. Figure 14 shows that the effect of J_{mi}/J_{cr} on $[P(I)-P(L)]/L$ also rapidly increases in the range of $R_i < 0.2$ mm. These results indicate that fiber radius may exert a dominant effect on the pressure drop per unit length of fiber and the effect of fiber length and J_{mi}/J_{cr} will sharply increase when the fiber radius is smaller than 0.2 mm.

The pressure drop per unit fiber length at the steady state (ΔP_f) is caused by fluid flow, membrane resistance, and cake resistance. The effect of cake resistance can be identified by comparing the pressure drops simulated by Eqs. 14 and 3. The former calculates pressures when cake deposits in regions where $J(x) > J_{cr}$. The latter represents the situation without deposition where the pressure drop (ΔP_w) is caused by fluid flow and membrane resistance. Figure 15 shows the effect of fiber length and radius on $(\Delta P_f - \Delta P_w)/\Delta P_w$. From

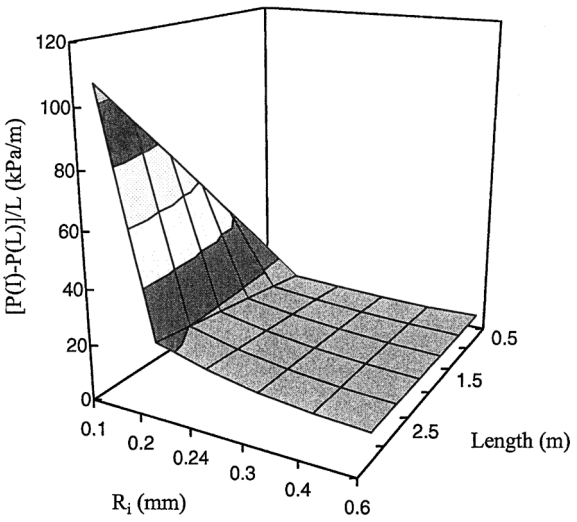

Figure 12. Simulated effect of fiber radius and length on $[P(I)-P(L)]/L$.

Simulation conditions: $J_{mi}/J_{cr} = 0.85$, $J_{cr} = 5.56 \times 10^{-6}$ m/s, $R_m = 10^{11}$ (l/m), $h = 0.5$ m, $g = 9.8$ m/s^2, $\rho = 1{,}000$ kg/m^3, $\mu = 0.001$ Ns/m^2.

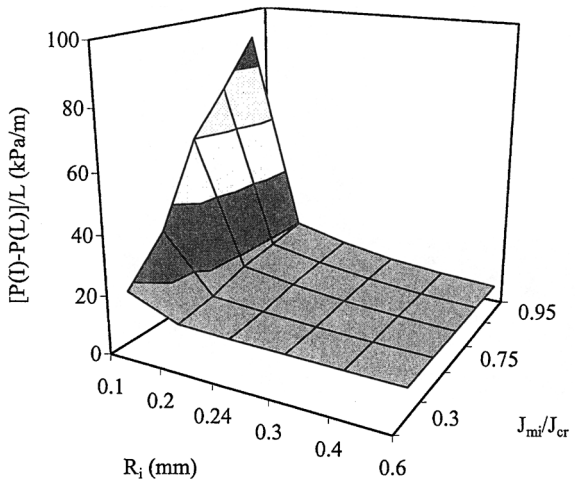

Figure 14. Simulated effect of fiber radius and J_{mi}/J_{cr} on $[P(I)-P(L)]/L$.

Simulation conditions: $L = 2$ m, $J_{cr} = 5.56 \times 10^{-6}$ m/s, $R_m = 10^{11}$ (l/m), $h = 0.5$ m, $g = 9.8$ m/s^2, $\rho = 1{,}000$ kg/m^3, $\mu = 0.001$ Ns/m^2.

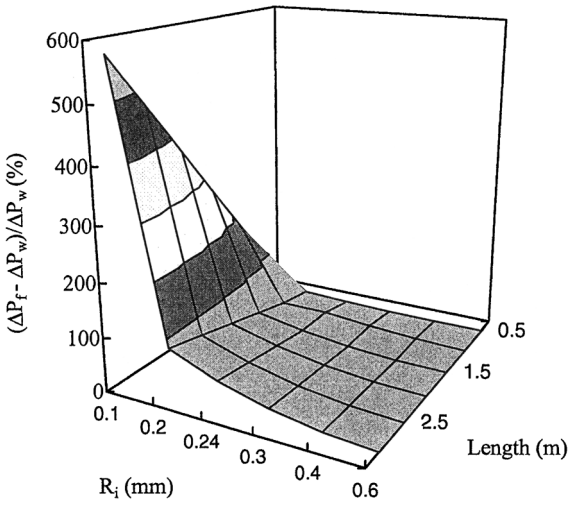

Figure 15. Simulated effect of fiber radius and length on $(\Delta P_f - \Delta P_w)/\Delta P_w$.

Simulation conditions: $J_{mi}/J_{cr} = 0.85$, $J_{cr} = 5.56 \times 10^{-6}$ m/s, $R_m = 10^{11}$ (l/m), $h = 0.5$ m, $g = 9.8$ m/s^2, $\rho = 1{,}000$ kg/m^3, $\mu = 0.001$ Ns/m^2.

this figure, it can be seen that the pressure drop caused by the initial deposition sharply increases when $R_i < 0.2$ mm. For example, for a 3 m long fiber with an inner radius 0.1 mm, the pressure drop per unit length caused by initial deposition is nearly 6 times higher than that caused only by membrane resistance and fluid flow. These analyses indicate that for long and small fibers ($R_i < 0.2$ mm), the initial deposition may result in significant increases in filtration resistance.

Optimization of fiber length and radius.

Packing Density. Traditionally, the packing density for the hollow fiber cartridge is defined as the filtration area provided by unit cartridge volume (Doshi et al., 1977). For the submerged system, the fiber bundle is directly submerged in the feed tank. The volume of the module seems no longer an appropriate characteristic parameter of the module. Thus, we define the filtration area provided by the unit cross section area of the head of the module as the packing density of the submerged hollow fiber module ($\phi = A_f/A_0$) (Figure 16). Based on an ideal triangular or square arrangement, the following can be deduced

$$\phi \propto \frac{L}{d_i + 2\delta} \tag{21}$$

Objective Function. Equation 21 shows that a small diameter and long fibers lead to a high packing density. For filtration with constant flux, high packing density increases the permeate flow rate per unit cross section area, provided the high packing density does not decrease the critical flux. On the other hand, however, small diameter and long fibers may lead to a greater axial pressure drop, which implies that more energy is needed to remove the permeate out of the fiber lumen. In order to balance the effect of the packing density and pressure drop on process efficiency, we define Eq. 22 as

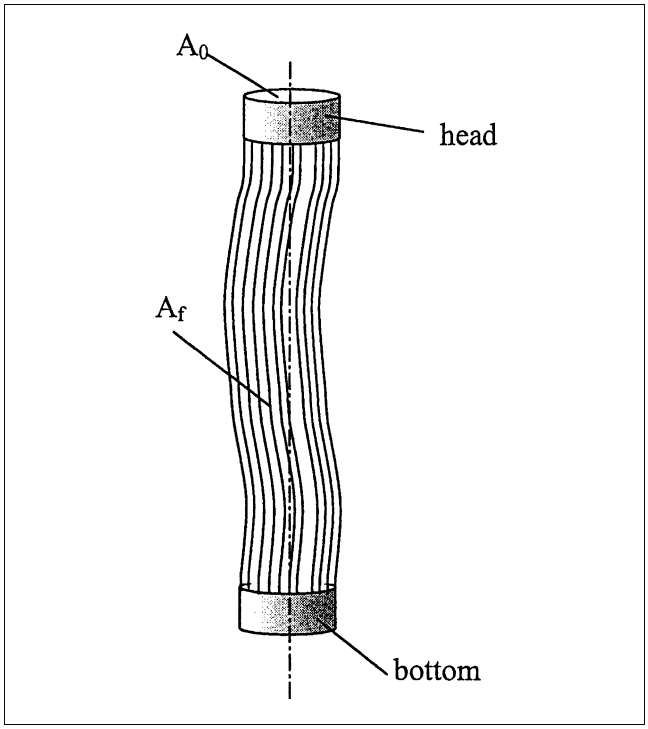

Figure 16. Fiber bundle.

the objective function for optimization of the fiber length and radius

$$Y = \left[\frac{J_{mi}\phi}{\Delta P_{\text{loss}}}\right] = \frac{J_{mi}L}{[P(I) - P(L)]\,(d_i + 2\delta)} = \frac{FJ_{cr}L}{[P(I) - P(L)]\,(d_i + 2\delta)} \tag{22}$$

The function Y can be regarded as the specific productivity of the permeate flow rate per unit cross section area of the module, per unit pressure drop along the fiber. The function neglects any pressure losses on the shell-side of the fiber and assumes that critical flux and fouling phenomena are similar for all fiber sizes. Figure 17 shows the simulated effect of fiber radius and length on the specific productivity Y. The simulation shows that the optimal fiber inner radius which slightly varies with the fiber length is around 0.2 mm. When the inner radius is smaller than 0.2 mm, Y decreases due to the sharply increased lumen pressure drop (Figure 12), while for $R_i > 0.2$, the specific productivity decreases due to the decreased packing density with the relatively large fiber radius. Figure 18 shows the optimal combination of fiber radius and length. From this figure, it can be seen that the optimal fiber radius increases with fiber length, indicating the competitive effect of packing density and pressure drop on the specific productivity. Comparing the specific productivity achieved with different combinations of fiber radius and length, the higher specific productivity goes to a small radius and short length with the maximum Y for the fiber with a radius of 0.21 mm and a length of 0.5 m. In addition, we can

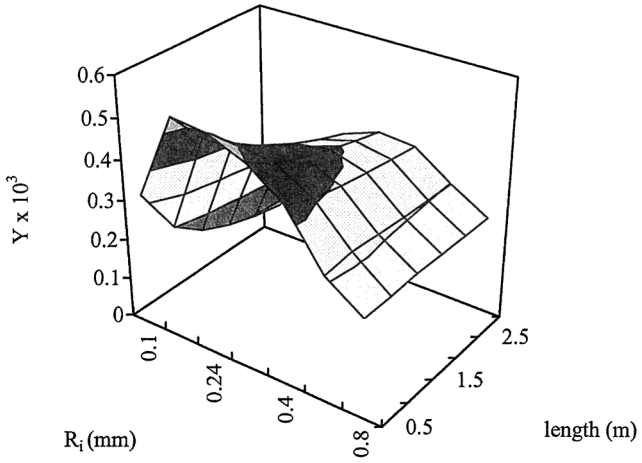

Figure 17. Effect of fiber length and fiber radius on specific productivity Y.

Simulation conditions: $J_{mi}/J_{cr} = 0.85$, $J_{cr} = 5.56 \times 10^{-6}$ m/s, $R_m = 10^{11}$ (l/m), $h = 0.5$ m, $\delta = 0.00035$ m, $g = 9.8$ m/s^2, $\rho = 1{,}000$ kg/m^3, $\mu = 0.001$ Ns/m^2.

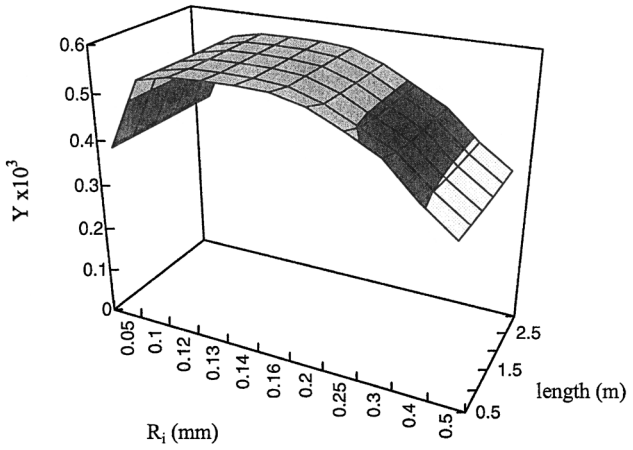

Figure 19. Effect of fiber length and radius on specific productivity Y.

Simulation conditions: $J_{mi} = 4.73 \times 10^{-6}$ m/s, $R_m = 10^{11}$ (l/m), $h = 0.5$ m, $g = 9.8$ m/s^2, $\rho = 1{,}000$ kg/m^3, $\delta = 0.00035$ m, $\mu = 0.001$ Ns/m^2.

see from the figure that the optimal fiber radius varies in a very narrow range from 0.21 to 0.3 when the length changes from 0.5 to 3 m. This implies that the fiber radius exerts a dominant effect on the specific productivity of the submerged system. The optimal diameter and maximum productivity are relatively insensitive to the actual critical flux. Simulations in which the critical flux is doubled predict a drop in the optimal diameter by less than 20% and a maximum productivity increase of less than 10%. In practice, other considerations, such as ease of manufacture and plant capacity, may determine the chosen fiber length. This analysis shows that there is an optimal fiber radius for a given fiber length.

Figure 19 shows the results simulated by Eq. 3 which does not consider the effect of initial deposition. Comparing these results with those in Figure 17, the optimal fiber radius goes to smaller values (around 0.13 mm) and the effect of fiber length nearly completely disappears. These differences are mainly due to the decreased effect of the pressure drop on Y for the situation without deposition.

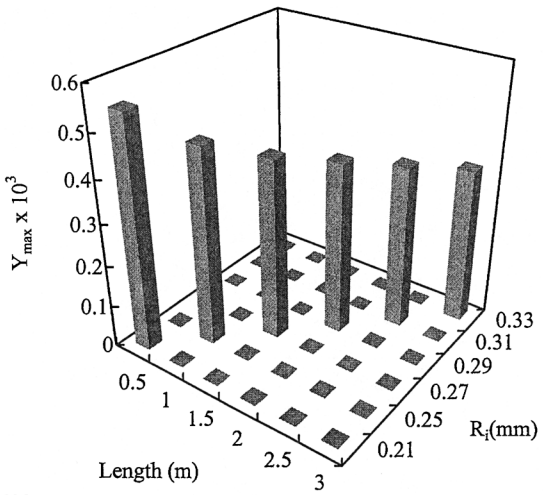

Figure 18. The optimal combination of fiber radius and length.

Simulation conditions: $J_{mi}/J_{cr} = 0.85$, $J_{cr} = 5.56 \times 10^{-6}$ m/s, $R_m = 10^{11}$ (l/m), $h = 0.5$ m, $\delta = 0.00035$ m, $g = 9.8$ m/s^2, $\rho = 1{,}000$ kg/m^3, $\mu = 0.001$ Ns/m^2.

Conclusions

Experimental observations of suction pressure history for different fluxes suggest scenarios where a steady state can be achieved when the imposed flux is controlled below the critical flux. Theoretical models have been developed for description of the filtration behavior of the submerged hollow fiber at steady state under these conditions. When the maximum initial flux is lower than the critical flux, no particle deposits on the membrane surface and the flux distribution can be described by models developed for filtration of pure water. For this situation, the value of $J_{i\max}/J_{mi}$ can be estimated according to a dimensionless parameter $\xi = 4LR_i^{-3/2}R_m^{-1/2}$. When the average imposed flux is lower than the critical flux, but the maximum local initial flux is higher than the critical flux, a steady state can be achieved after an initial deposition. The length with initial deposition depends on the ratio of J_{mi}/J_{cr}, fiber radius, length, and membrane permeability. The filtration resistance caused by the initial deposition becomes significant when the fiber radius is smaller than 0.2 mm, particularly with long lengths and high J_{mi}/J_{cr}. The developed models have been used to optimize fiber length and radius through maximizing the specific productivity. The simulation suggests that the optimal combination of fiber radius and length goes to small radius and short length. The optimal fiber radius for fiber lengths from 0.5 to 3 m is determined in the range of 0.2 to 0.35 mm.

Notation

A_f = filtration area, m^2
A_0 = section area of fiber bundle, m^2
C_1 = constant
C_2 = constant
d_o = fiber outer diameter, m
F = ratio of J_{mi}/J_{cr}
g = gravity acceleration, m/s^2

h = submerged depth of the fiber, m
J_{cr} = critical flux, m/s
$J_{i\max}$ = maximum initial flux at fiber outlet, m/s
J_{mi} = average imposed flux based on the inner fiber area, m/s
J'_{mi} = average imposed flux based on the inner fiber area over the length of the fiber without deposition (Figure 3b), m/s
L = fiber length, m
L_h = fiber length where flux is higher than the average imposed flux, m
$P(I)$ = gauge pressure at the fiber dead-end (reference pressure atmospheric), N/m^2
$P(L)$ = gauge pressure at the outlet of the fiber, N/m^2
$p(x)$ = gauge pressure of permeate flow in the fiber lumen at x coordinate (reference pressure atm), N/m^2
ΔP_f = pressure drop per unit length along fiber lumen at the steady state with deposition, Pa/m
ΔP_W = pressure drop per unit length along fiber lumen for filtration without deposition, Pa/m
r = radial coordinate
R_i = fiber inner radius, m
R_m = membrane resistance, l/m
R_t = total filtration resistance, l/m
R_c = cake resistance, l/m
u = axial velocity of the flow in the fiber lumen, m/s
v = radial velocity of the flow in the fiber lumen, m/s
V_g = gas-flow rate, L/min
x = axial coordinate
x' = axial coordinate in the range of $x_{cr} \le x \le L$ (Figure 3b)
x_{cr} = length of the fiber without deposition (Figure 3b)
Y = specific productivity per unit pressure drop per unit potting area of module, m^3/s/kPa/m^2

Greek letters

δ = fiber thickness
ϕ = fiber packing density of submerged hollow fiber module
λ = coefficient
μ = viscosity of fluid, Ns/m^2
ξ = coefficient
ρ = density of fluid, kg/m^3

Acknowledgments

Support for this study by Anjou Recherche, General Water Australia and US Filter, is gratefully acknowledged

Literature Cited

Apelblat, A., A. Katzir-Katchalsky, and A. Silberberg, "A Mathematical Analysis of Capillary-Tissue Fluid Exchange," *Biorheology*, **11**, 1 (1974).

Belfort, G., R. H. Davis, and A. L. Zydney, "Review: The Behavior of Suspensions and Macromolecular Solutions in Crossflow Microfiltration," *J. Memb. Sci.*, **96**, 1 (1994).

Bruining, W. J., "A General Description of Flows and Pressures in Hollow Fiber Membrane Modules," *Chem. Eng. Sci.*, **44**, 1441 (1989).

Chang, S., and A. G. Fane, "The Effect of Fibre Diameter on Filtration & Flux Distribution—Relevance to Submerged Hollow Fibre Modules," *J. Membrane Sci.*, **184**(2), 221 (2001).

Doshi, M. R., W. N. Gill, and V. N. Kabadi, "Optimal Design of Hollow Fibre Modules," *AIChE J.*, **23**, 765 (1977).

Field, R. W., D. Wu, J. A. Howell, and B. B. Gupta, "Critical Flux Concept for Microfiltration Fouling," *J. Memb. Sci.*, **100**, 259 (1995).

Günder, G., and K. Krauth, "Replacement of Secondary Clarification by Membrane Separation—Results with Plate and Hollow Fibre Modules," *Wat. Sci. Tech.*, **38**, 383 (1998).

Kelsey, L. J., M. R. Pillarella, and A. L. Zydney, "Theoretical Analysis of Convective Flow Profiles in a Hollow-Fibre Membrane Bioreactor," *Chem. Eng. Sci.*, **45**, 3211 (1990).

Li, H., A. G. Fane, H. G. Coster, and S. Vigneswaran, "Direct Observation of Particle Deposition on the Membrane Surface During Crossflow Microfiltration," *J. Memb. Sci.*, **149**, 83 (1998).

Ohmori, H., T. Yahashi, Y. Furukawa, K. Kawamura, and Y. Yamamoto, "Treatment Performance of Newly Developed Johkasou with Membrane Separation-on-Site System for Domestic Sewage Treatment in Japan," *Proc. of Memb. Technol. in Environ. Management*, Tokyo, Japan, 38 (1999).

Parameshwaran, K., A. G. Fane, B. D. Cho, and K. J. Kim, "Analysis of Microfiltration Performance with Constant Flux Processing of Secondary Effluent," *Wat. Res.*, **35**(18), 4349 (2001).

Serra, C., M. J. Clifton, P. Moulin, J-C. Rouch, and P. Aptel, "Dead-end Ultrafiltration in Hollow Fibre Modules: Module Design and Process Simulation," *J. Memb. Sci.*, **145**, 159 (1998).

Ueda, T., and K. Hata, "Domestic Wastewater Treatment by a Submerged Membrane Bioreactor with Gravitational Filtration," *Wat. Res.*, **33**, 2888 (1999).

Manuscript received Aug. 30, 2001, and revision received Feb. 25, 2002.